University of Colorado at Boulder

Honors Thesis

Autocorrelation of Photoemission Self Energy to Quasiparticle Interference in $Bi_2Sr_2CaCu_2O_{8+\delta}$

Author:
Matthew Cavenaugh Kilpatrick

Advisor:
Professor Dan Dessau and
Assistant Professor Kyle
McElroy

A thesis submitted in fulfilment of the requirements
for the degree of Bachelors of Arts

in the

Dessau Group
Department of Physics

April 2014

Declaration of Authorship

I, Matthew Cavenaugh Kilpatrick, declare that this thesis titled, 'Autocorrelation of Photoemission Self Energy to Quasiparticle Interference in $Bi_2Sr_2CaCu_2O_{8+\delta}$' and the work presented in it are my own. I confirm that:

- This work was done wholly or mainly while in candidature for a research degree at this University.
- Where I have consulted the published work of others, this is always clearly attributed.
- Where I have quoted from the work of others, the source is always given. With the exception of such quotations, this thesis is entirely my own work.
- I have acknowledged all main sources of help.
- Where the thesis is based on work done by myself jointly with others, I have made clear exactly what was done by others and what I have contributed myself.

Signed: _____

Date: _____

Committee Members

Professor Dan Dessau:

Assistant Professor Kyle McElroy:

Professor Paule Beale:

Professor Andrew Hamilton:

UNIVERSITY OF COLORADO AT BOULDER

Abstract

Professor Dan Dessau
Department of Physics

Bachelors of Arts

Autocorrelation of Photoemission Self Energy to Quasiparticle Interference in $\mathbf{Bi_2Sr_2CaCu_2O_{8+\delta}}$

by Matthew Cavenaugh Kilpatrick

The photoemission self energy (PLL) model describes the energy and temperature dependence of cuprate superconductors as a function of doping. Currently the theory has only been applied to the superconducting state for $Bi_2Sr_2CaCuO_{8+\delta}$ (Bi-2212). By applying an autocorrelation with Fourier transforms, we hope to describe the temperature and energy dependence of quasiparticle interference for three different doping values of Bi-2212 at, $\delta = 0.11$ under-doped, $\delta = 0.16$ optimally doped, and $\delta = 0.21$ over-doped. The various effects of tracking the magnitudes of the **q**-vectors are discussed and three different analysis methods are used. A discussion in the differences between two types of reconstruction is included along with an analysis of why the QPI method of gap analysis is inconsistent with the density of states method.

Acknowledgements

Thank you to Professor Dan Dessau and Assistant Professor Kyle McElroy for helping me along the way with this project. Thank you to Steve Parham, Justin Waugh, Haoxiang Li and all the other graduate student in lab for helping me understand all the necessary material. Thank you to my parents for supporting me throughout the entire process.

Contents

List of Figures

Chapter 1

Introduction to Photoemission Self Energies and Quasiparticle Interference

Fermi liquid self energy is a topic that is well understood in condensed matter physics. This theory explains many properties such as specific heat and resistivity of most metals. Unfortunately, this model in unable to explain some properties seen in certain metals, such as quantum critical points in high T_c cuprate superconductors [1].

The photoemission self energy (PESE) phenomenology is a new way to express the energy and temperature dependence of cuprate superconductors, while including the dependence on doping. We have fitted it to express the superconducting state conditions for Bi-2212. In this paper, we use this new form of the self energy, developed by Dessau Group, to describe the energy and temperature dependence of quasiparticles in the lattice of Bi-2212.

The lattice of cuprate superconductors is stationary (when phonons are neglected). Free electrons move as waves within the structure and scatter off inhomogeneities, causing the electron's momentum eigenstates to mix and produce modulations in the wave pattern [2]. These modulations can be Fourier transformed and viewed as the scattering of an electron with some momentum $\mathbf{k}_i$ to another with momentum $\mathbf{k}_f$. Using the octet model, we describe these scattering electrons as vectors, $\mathbf{q} = \mathbf{k}_f - \mathbf{k}_i$. The octet model is used to look at the origin of quasiparticle interference (QPI) and how it can be described as the scattering of electrons in momentum space. This model shows that QPI is the same as a mixing of eigenstates for electrons on the edges of "bananas" or "Fermi arcs".

Quasiparticles are used in many-body physics—multiple particles in a single system—to describe the properties of multiple particles acting as one. In a solid, the quasiparticles are many electrons moving as waves throughout the structure of the lattice, the atomic nuclei. Since QPI is responsible for key electrodynamic features in cuprate superconductors, we want to understand their properties and origins to further our understanding of solids. We will first examine varying Fermi liquid phenomenology and its properties, then we will look at the QPI properties of Bi-2212. Finally, we will show that through the application of this model, we can explain some previously unexplained properties.

Chapter 2

Photoemission Self Energies

The PESE phenomenology is a power law liquid self energy with additional terms for Bi-2212. We introduce the imaginary self energy and its application to the spectral function. This will then be applied in an autocorrelation to analyze the QPI for Bi-2212. The following is provided by communication with Professor Dan Dessau and Dessau Group since, the self energy being discussed has not been published yet.

2.1 Self Energy

The power law liquid (PLL) model is a phenomenology in development by the Dessau group at the University of Colorado at Boulder to show the energy and temperature dependence of cuprate superconductors for different oxygen doping values. Initially, we had the Fermi liquid model, which does not account for the doping of the solid. The contribution to the electron's energy due to interactions with the system is the self energy which goes as,

$$\Sigma'' = C(\omega^2 + (\pi T)^2), \tag{2.1}$$

where Σ'' is the imaginary part of the self energy, ω is the energy, T is the temperature, and C is a constant for normalization [3]. The varying Fermi liquid model adds to this self energy as follows,

$$\Sigma'' = \Gamma_0 + \lambda \frac{(\omega^2 + (\beta k_B T)^2)^\alpha}{\omega_N^{2\alpha-1}}. \tag{2.2}$$

We have Γ_0 to account for impurity scattering, λ as a coupling parameter which shows the strength of the scattering, ω_N as the normalization frequency where the exponent preserves the dimensions of the self energy, β controls the strengths of the temperature and energy, and α as the main variable that controls whether the solid should be viewed as a Fermi liquid, marginal Fermi liquid, or a power law liquid. Equation 2.2 shows a

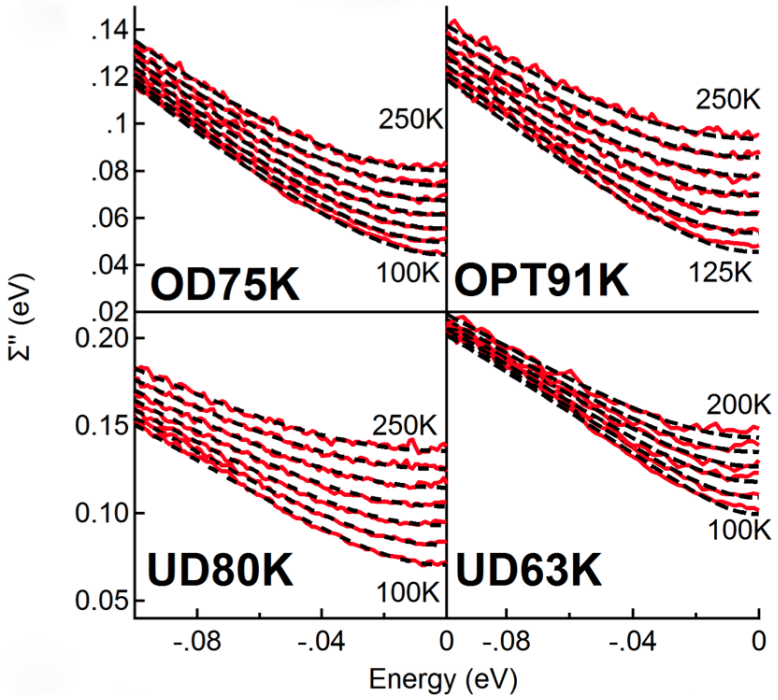

FIGURE 2.1: Measured temperature and energy dependence of the self energy for four samples from overdoped T_c=75K (OD75K) to optimal doped T_c=91K (OPT91K) to underdoped T_c=63K (UD63K). The data was fitted at constant temperature for each scenario. This graphic is courtesy of Dessau group at University of Colorado at Boulder.

linear dependence in temperature in the superconducting state, when $\alpha = \frac{1}{2}$, which is contradictory to the Fermi liquid theory predicted by Landau [4].

The self energy fits for the data show a linear dependence in temperature for large energy values arises from α having a value near $\frac{1}{2}$ for most doping values (see fig. 2.2, 2.1). The fitted data show that λ and β are practically independent for all doping values and that α is linear with doping. We have determined the values of λ, β, and Γ to be 1, π, and a range of 3 to 10 meV, respectively (see fig. 2.2). This data from photoemission holds for the superconducting state of an optimally doped Bi-2212. Since this is only the imaginary portion of the self energy, the Kramers-Kronig relation is used to get the real part. Once we have both parts of the self energy, we can then include it in the spectral function.

2.2 Additional Functions Added to Power Law Liquid

A kink is subtracted from the self energy because the spectra of Bi-2212 shows a coupling of electrons to a bosonic phase, which are phonons. A hump is also added to the self energy to match experimental data seen in the sprectra that cannot be explained with theory at the moment. The kink for this spectra turns out to be a negative kink since, it

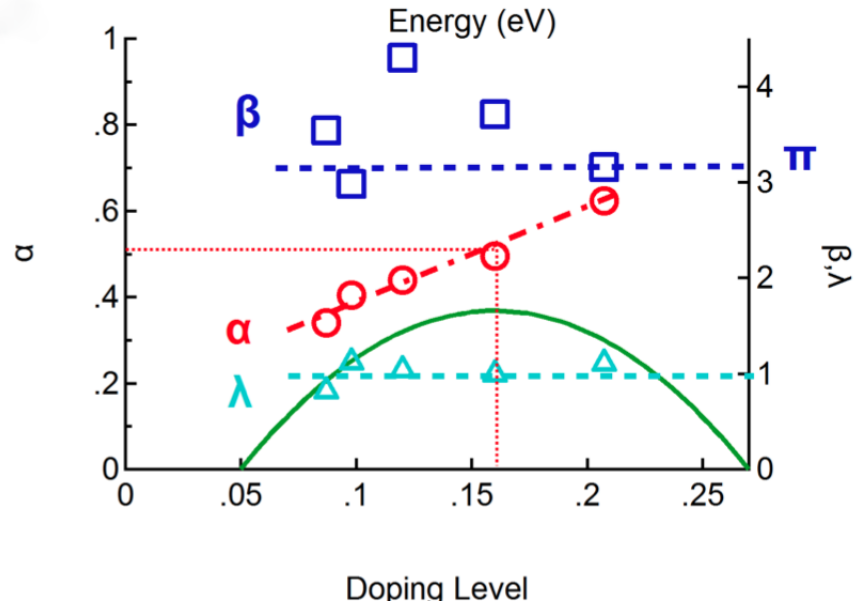

FIGURE 2.2: Fit results for the three main parameters in the model as a function of doping. The superconducting dome is schematically illustrated by the inverted parabola. The most relevant parameter is the power α which is linear as a function of doping with value 0.5 very near optimal doping. Graphic courtesy of Dessau Group at University of Colorado at Boulder.

negates the self energy below some value in energy. The kink is essentially a Fermi-Dirac distribution and is as follows,

$$Kink = \frac{Kink_1 * k_B * T_c}{\exp\left(\frac{|x| - Kink_E}{k_B * Kink_{W_0}}\right) + 1}, \tag{2.3}$$

where $Kink_E$ is the energy where the kink will start (and is analogous to ϵ in the Fermi-Dirac distribution), $Kink_{W_0}$ is essentially the intensity of the step function (and is analogous to T), $Kink_1$ is a fitted parameter to indicate the magnitude of the kink, and T_c is the critical temperature for Bi-2212, which is the temperature at which it starts to superconduct [5].

The hump is added to the PLL in the form of a gaussian and is,

$$Hump = Hump_1 * \exp\left(\frac{-(x - Hump_E)^2}{2 * Hump_w^2}\right), \tag{2.4}$$

where $Hump_1$ is the maximum, $Hump_E$ is the energy at which the hump is centered, and $Hump_w^2$ is the variance (see fig. 2.3). The physical significance of this new self energy is still in progress for the Dessau Group, but it is used to match experimental data that is seen in the spectra of Bi-2212.

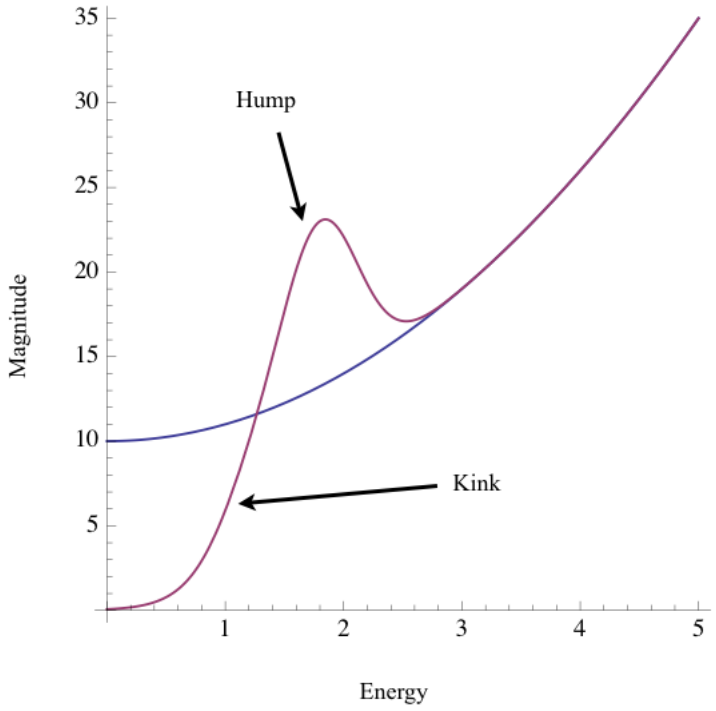

FIGURE 2.3: In blue, is a profile an arbitrary self energy with ω^2 dependence, such as Fermi liquid. In purple, is the additions to the self energy. The kink pushes the self energy towards zero for low energy and hump is added as a gaussian.

2.2.1 Spectral Function

The bare band structure of Bi-2212 is expressed mathematically as,

$$\begin{aligned}\xi_k =& t_0 \\ &- 2t_1 * [\cos(k_x) + \cos(k_y)] \\ &- 4t_2 * \cos(k_x)\cos(k_y) \\ &- 2t_3 * [\cos(2k_x) + \cos(2k_y)] \\ &- 4t_4 * [\cos(2k_x)\cos(k_y) + \cos(k_x)\cos(2k_y)],\end{aligned} \tag{2.5}$$

where t_i are constants determined by theory, and the k_x and k_y are the x and y momentums respectively [6]. This is plotted in Mathematica to give a visual representation of the band structure (see fig. 3.2). Using the Nambu-Gorkov formalism, we can calculate the spectral function.

The Nambu-Gorkov formalism is used to express the spectral function first as zero points. We can first write the inverse of the green's function as,

$$G^{-1}(\mathbf{k},\omega) = \begin{bmatrix} \omega - \xi_k - \Sigma & Re(Z)\Delta_k \\ Re(Z)\Delta_k & \omega + \xi_k - \Sigma \end{bmatrix}, \tag{2.6}$$

where ξ_k is the bare band structure (see Eq. 2.5), ω is energy, Z is a renormalization factor for the paired electrons (see eq. 4.3), Σ is the real and imaginary part of the self energy, and

$$\Delta_k = \frac{\Delta_0}{2}[\cos(k_x) - \cos(k_y)] = \frac{\Delta_0}{2}\cos(\theta_k) \tag{2.7}$$

is the function of the superconducting gap, where Δ_0 is the maximum gap, θ_k is the angle from the node with respect to the corners of the Brillouin zone, and k_x and k_y are the components of momentum. From here inverting Eq. 2.6 yields the green's function,

$$G(\mathbf{k},\omega) = \frac{1}{(\omega-\Sigma)^2 - \xi_k^2 - Re(Z)^2\Delta_k^2}\begin{bmatrix} \omega+\xi_k-\Sigma & -Re(Z)\Delta_k \\ -Re(Z)\Delta_k & \omega-\xi_k-\Sigma \end{bmatrix}. \tag{2.8}$$

In the inverse of the Green's function there will be a pole whenever the determinant is zero, which will indicate that an electron (or hole) is present [7].

Using the imaginary part of the electron Green's function we can calculate the spectral function of Bi-2212 that is used for Angle Resolved Photoemission Sprectroscopy (ARPES),

$$A(\mathbf{k},\omega) = \frac{-1}{\pi} Im \frac{\omega+\xi_k-\Sigma}{(\omega-\Sigma)^2 - \xi_k^2 - Z^2\Delta_k^2}. \tag{2.9}$$

This is used to compute the density of states in $\mathbf{k}$-space and is used in the autocorrelation of Bi-2212. ARPES is the experiment that is used to retrieve the momentum space data for Bi-2212. The Oli Anderson matrix element from scanning tunneling microscopy (STM) experimental data is added to the spectral function to match STM autocorrelation and is as follows,

$$M = |\cos(k_x) - \cos(k_y)|, \tag{2.10}$$

where k_x and k_y are the x and y momentums, respectively [8]. The new additions to the PLL model are now added to the self energy to match experimental data.

Chapter 3

Properties of Quasiparticle Interference

The background of quasiparticle interference (QPI) in discussed. The background does not take into account self energies. The factors leading to the octet model are introduced and explained.

3.1 The Octet Model and the Density of States

Crystalline solids are lattices, nuclei of atoms sitting in a periodic orientation. These lattices are known to repeat and can viewed as a primitive unit cell repeated throughout the material. The primitive unit cell is the smallest volume of the lattice that describes the entire material.

Electrons move as waves throughout the lattice of Bi-2212. Due to irregularities in the lattice, the unit cells are not perfectly stacked over each other. The eigenstates of the electrons interfere with each other, causing modulations. These modulations can be Fourier transformed into vectors in the Brillouin zone—the primitive cell transformed into momentum space. The octet model is used to visualize the vectors as the scattering of electrons from one point to another in momentum space. These points are determined by the density of states for the bare band structure for $Bi_2Sr_2CaCuO_{8+\delta}$ [9, 10].

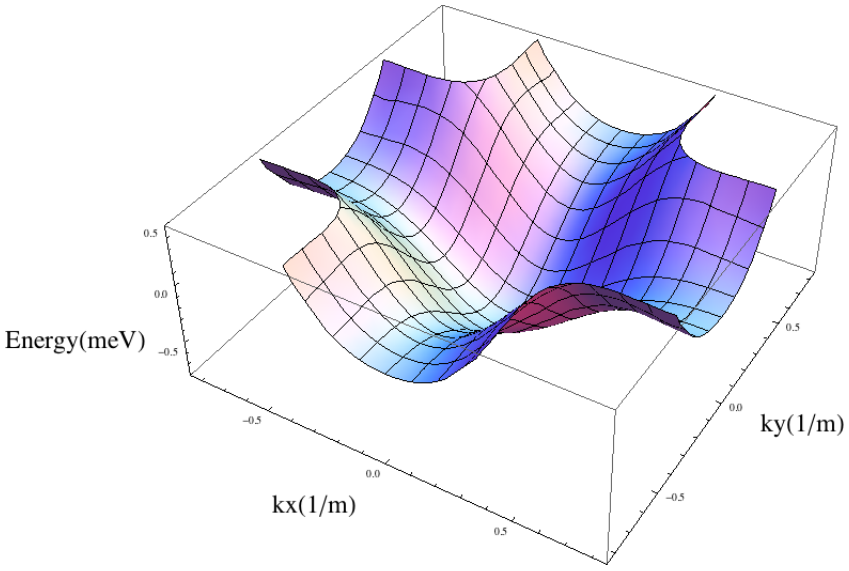

FIGURE 3.1: The bare band stucture of Bi-2212 in the normal state. The plot is made such that the Fermi energy is zero.

3.1.1 Density of States

The density of states (DOS) is defined as the number of states per unit energy. This is determined by,

$$D(\omega) = \frac{d\Omega_n}{d\omega}, \tag{3.1}$$

where Ω_n is the number of states at a certain energy in the Brillouin zone and ω is the energy. The DOS is caused by the back-bending of the bare band structure and coherence factors.

Back-bending of the bare band structure is caused by the superconducting gap. The band structure is a representation of the energy of an electron at a certain momentum. We imagine the electrons actually sitting on the band structure itself. Once the material begins to superconduct, the superconducting gap forms, causing the band structure to change from the normal state (fig. 3.1) and bend back on itself, (see fig. 3.2). Electrons are then able to occupy these new available states. The two halves of fig. 3.2 correspond to electron states and hole states, the absence of an electron, which are the bottom and top respectively. These two halves of the band structure are touching at the node. The coherence factors will give the respective probability of a state being available on the band.

The coherence factors,

$$v_k^2 = \frac{1}{2}\left(1 - \frac{\xi_k}{\sqrt{\Delta_k^2 + \xi_k^2}}\right), \tag{3.2}$$

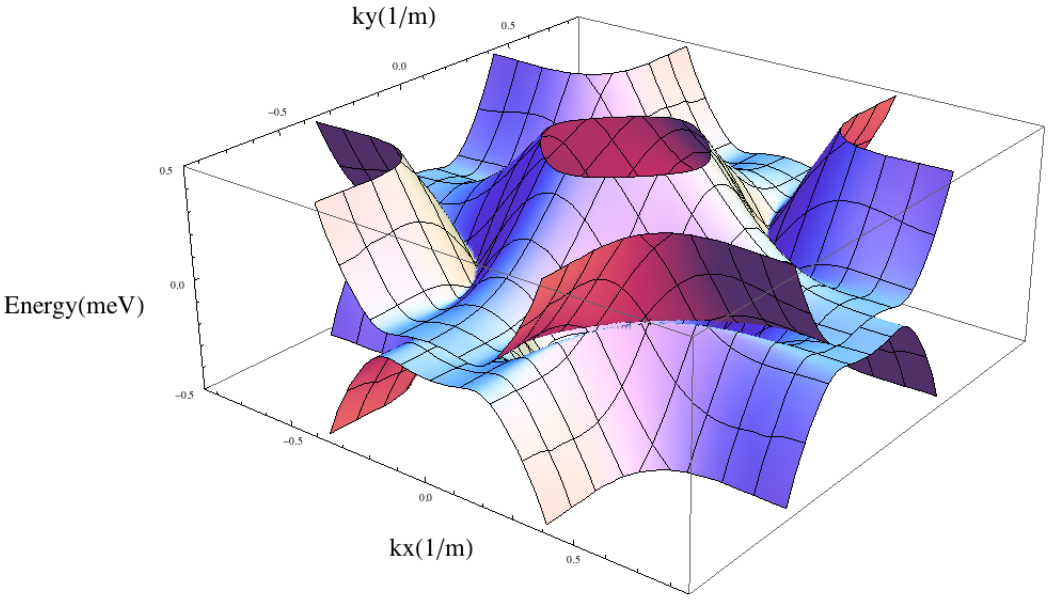

FIGURE 3.2: The band structure for $Bi_2Sr_2CaCuO_{8+\delta}$ where the horizontal axes are the x and y components of the momentum with the origin at the center. The vertical axis is energy, in meV, with the Fermi energy at zero. The band structure bends back when it gets to the Fermi energy with a superconducting gap and the allowed states are given by the coherence factors.

$$u_k^2 = \frac{1}{2}\left(1 + \frac{\xi_k}{\sqrt{\Delta_k^2 + \xi_k^2}}\right), \tag{3.3}$$

where ξ_k is the band structure, Δ_k is the superconducting gap, and v_k^2 and u_k^2 are the electron and hole probabilities, respectively [7]. The Nambu-Gorkov formalism has these probabilities already in the equations. At an energy smaller than the Fermi energy, which is chosen to be zero, the electrons have a higher probability of being in the inner bowl of the band as opposed to the outside slopes of the band, (see fig. 3.3) where only the band for the electron states is shown [10]. When the energy is close to the Fermi energy the probability of the states being on either side is roughly the same. When combined, these effects will cause the density of states to be on the edges of the "bananas" or "Fermi arcs". Fig. 3.4 gives a 2D representation of the band structure with contours of energy. At the edges the rate of change of the energy is minimal which causes a maximum in electron states Eq. 3.2 and 3.3, (see fig. 3.2, 3.4). These effects are already implemented in the Nambu-Gorkov formalism and the spectral function. The octet model uses these points of higher density of states as the beginning and ending points for the scattering electrons, $\mathbf{q} = \mathbf{k}_f - \mathbf{k}_i$.

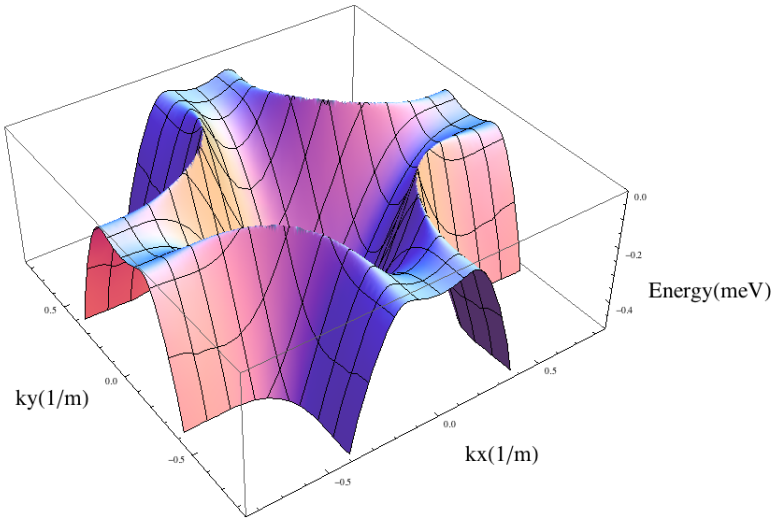

FIGURE 3.3: The bottom half of the band structure corresponding to electron states. At any energy the inner portion of the band has a higher probability of an electron being there than the outer band does. Near the Fermi surface these probabilities approach each other and and electron can be on either side of the band.

3.2 Octet Model

In fig. 3.4, the band structure has four "bananas" where on the edges of them is the highest DOS. The octet model says that an electron can scatter from any one of the points of highest DOS to any of the others. This process is described by $\mathbf{q}$ vectors that point from one point to another. Since each point has seven possible $\mathbf{q}$ (see fig. 3.4),

$$\begin{aligned}
\mathbf{q}_1 &= (2k_x, 0) \\
\mathbf{q}_2 &= (k_x + k_y, k_y - k_x) \\
\mathbf{q}_3 &= (k_x + k_y, k_y + k_x) \\
\mathbf{q}_4 &= (2k_x, 2k_y) \\
\mathbf{q}_5 &= (0, 2k_y) \\
\mathbf{q}_6 &= (k_x - k_y, k_y + k_x) \\
\mathbf{q}_7 &= (k_x - k_y, k_y - k_x),
\end{aligned} \tag{3.4}$$

and there are eight total points, then the total possible vectors is $7 \times 8 = 56$. Then using the eight fold symmetry of the Fermi surface, the fact that mathematically there is no difference between $\mathbf{q}$ and $-\mathbf{q}$, and that $\mathbf{q}_2$ is rotated by 90 degrees compared to $\mathbf{q}_6$ all cause the number of independent $\mathbf{q}$-vectors to six [8, 10, 11]. The octet model is used to explain some properties of Bi-2212, but others have yet to be explained.

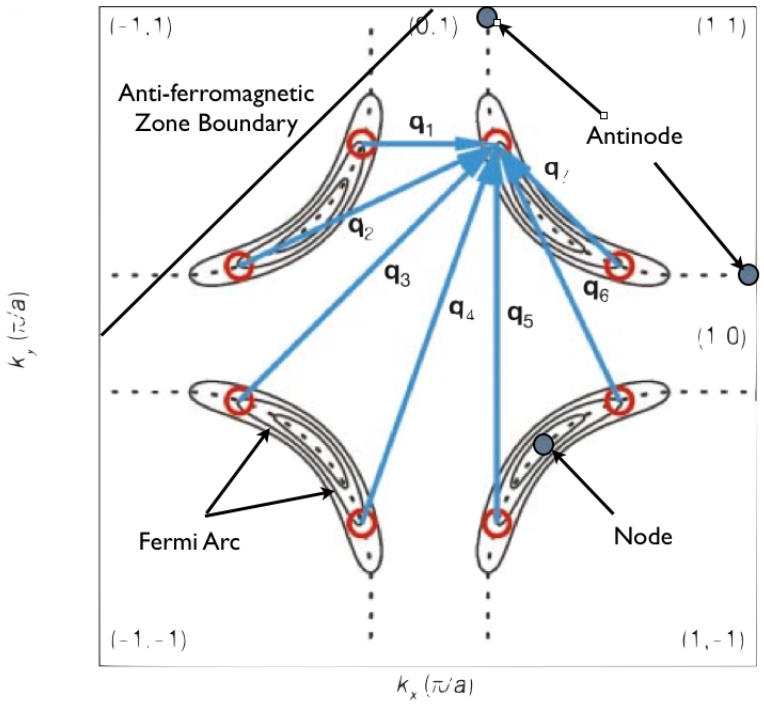

FIGURE 3.4: The Brillouin zone for $Bi_2Sr_2CaCuO_{8+\delta}$. The blue arrows indicate the **k**-space locations of several banana-shaped quasiparticle contours of constant energy as they increase in size with increasing energy. The antinodes are shown at the edge of the zone and by symmetry there are two for every Fermi arc, also the node is located in the middle of the Fermi arc. As an example, at a specific energy, the octet of regions of high $\mid \Delta_k E(\mathbf{k}) \mid^{-1}$ are shown as red circles. The seven primary scattering q-vectors interconnecting elements of the octet are shown in blue. Adapted from [8]

3.3 Properties Verified with Current Model

The Octet model has led to the verification of many properties for QPI. QPI imaging has the rare ability to determine the electronic structure of the cuprate superconductor in real space and in momentum space. Since it is the Fourier transform of the modulations in real space to momentum space, it provides access to the band structure and lattice information at the same time. The octet model has helped with some main aspects of QPI.

First, the octet model can describe how QPI agrees with ARPES data and shows that the nanoscale electronic disorder that was detected previously by Scanning Tunneling Spectroscopy (STS) [8]. Also, the intensities of the modulations between the k-space regions that have the same sign and d-wave order parameter are maintained, while the intensities of those with different signs are decreased [12].

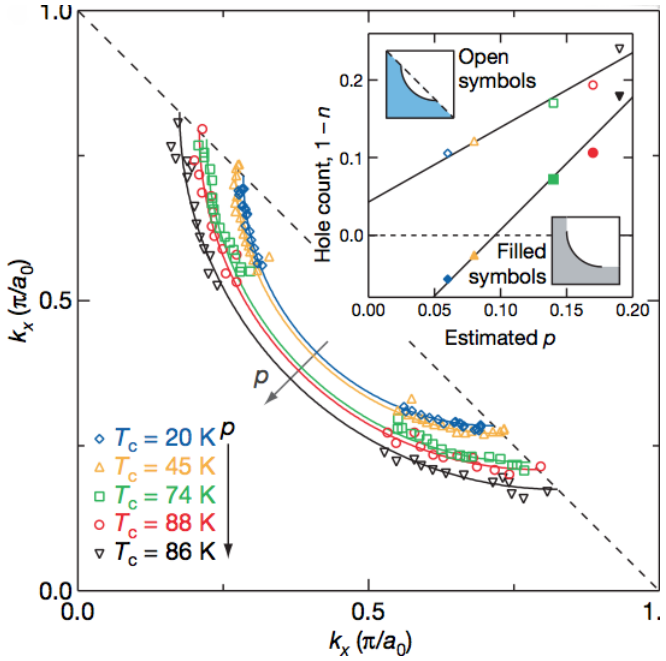

FIGURE 3.5: The anti-ferromagnetic zone boundary is the line joining the points $(\pm\pi, 0)$ and $(0, \pm\pi)$. It is seen experimentally that the **q**-vectors stop at this line for most temperatures [11]

3.4 Properties not yet Verified with Current Model

While we have learned much from the Octet model there are three questions that have not been answered. First, it is unknown why QPI disappears near the anti-ferromagnetic zone boundary, the line that connects the point $(\pm\pi, 0)$ and $(0, \pm\pi)$ in the Brillouin zone (see fig. 3.4, 3.5) [11]. Second, the temperature dependence of QPI shows the superconducting gap closing near the node (see fig. 3.6) [12]. Finally, there is a static nature of the q_1 vector that does not change with temperature where the other q-vectors are dependent [13]. It is possible that the PESE phenomenology will be able to explain why these properties occur for QPI in Bi-2212.

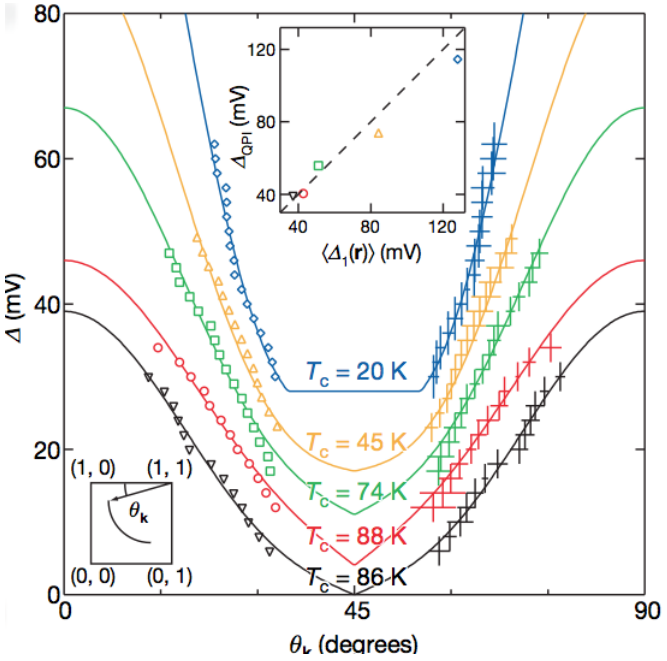

FIGURE 3.6: The QPI is seen to collapse at the node as temperature is decreased. The shift in the graphs is given for clarity where θ is the angle with respect to the anti-node and Δ is the gap magnitude [11].

Chapter 4

Methods

In this chapter is a discussion of the processes for the project. First, we simulate PESE for three different doping and interpolating to get a function for all k-space and energy. Then autocorrelate the spectral function and analyzing the energy dependence of the peaks that arise which are directly related to QPI in the octet model. The four methods of analysis, DOS, tracking **q**-vector slopes and intersection, recreating the Brillouin zone, and plotting the output gap using QPI are introduced and explained

4.1 Methods

4.1.1 Adding the Self Energy

The self energy used here is PLL with a kink and a hump added. This self energy is dependent on energy and momentum (see fig. 5.1). The position of the five cuts for PESE were determined by Haoxiang Li and is given by

$$k_{||} = \sqrt{2mE}\sin\theta, \tag{4.1}$$

where m is the mass of an electron, E is the energy of the electron after the binding energy is subtracted, and θ is the angle with respect to the node angle. We know the self energy at five locations in the Brillouin zone starting at the node and ending at the anti-node thanks to Haoxiang Li. These values are then interpolated and symmetry is used to acquire the value of the self energy at all points in k-space.

In chapter 2, the imaginary portion of the self energy was introduced (see Eq. 2.2, 2.3, 2.4). We now want the full expression so that it can be included in the green's function. We have the values of the self energy for five cuts in the Brillouin zone. These cuts must

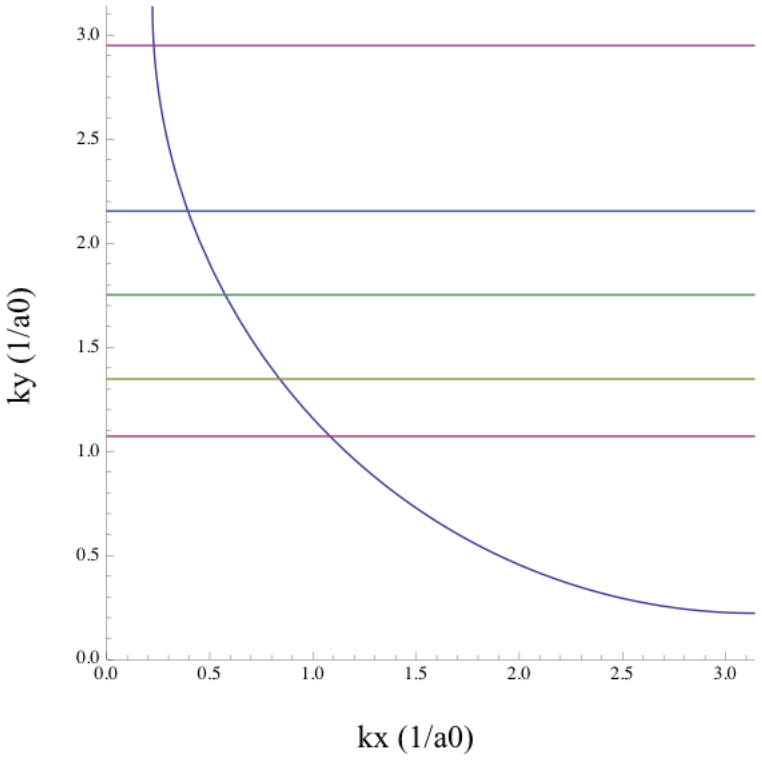

FIGURE 4.1: The positions of the PESE simulations are shown with respect to the fermi surface of Bi-2212. These cuts are then interpolated and the symmetry of the Brillouin zone is used the achieve a self energy for the entire zone.

be interpolated to give the values of the self energy for the entire Brillouin zone. This will give the imaginary part of the self energy for all values of energy and momentum. The real part of the self energy is found by using the Kramers-Kronig relation,

$$\begin{aligned} \Sigma'(\omega) =& \frac{1}{\pi} P \int_{-\infty}^{\infty} \frac{\Sigma''(\omega')}{\omega' - \omega} d\omega' \\ \Sigma''(\omega) =& \frac{-1}{\pi} P \int_{-\infty}^{\infty} \frac{\Sigma'(\omega')}{\omega' - \omega} d\omega', \end{aligned} \tag{4.2}$$

where Σ' and Σ'' are the real and imaginary parts of a complex function Σ, P is a Cauchy principal value, and the integrals are taken over all values of ω'. The Kramers-Kronig relation is used to find the real (or imaginary) part of a complex function. The Kramers-Kronig relation is only valid for functions that can be locally defined by a power series that converges [14]. We use this on the self energy to find the real part.

The process of actually calculating the real part of the self energy was simplified by Justin Waugh and Haoxiang Li. They developed a program that will convolve the function point-by-point and has a smaller computation time than computing the integral flat out. The calculation of the renormalization factor, Z, is done by first doing Kramers-Kronig relation on the five cuts of the imaginary part of the self energy. Then using the

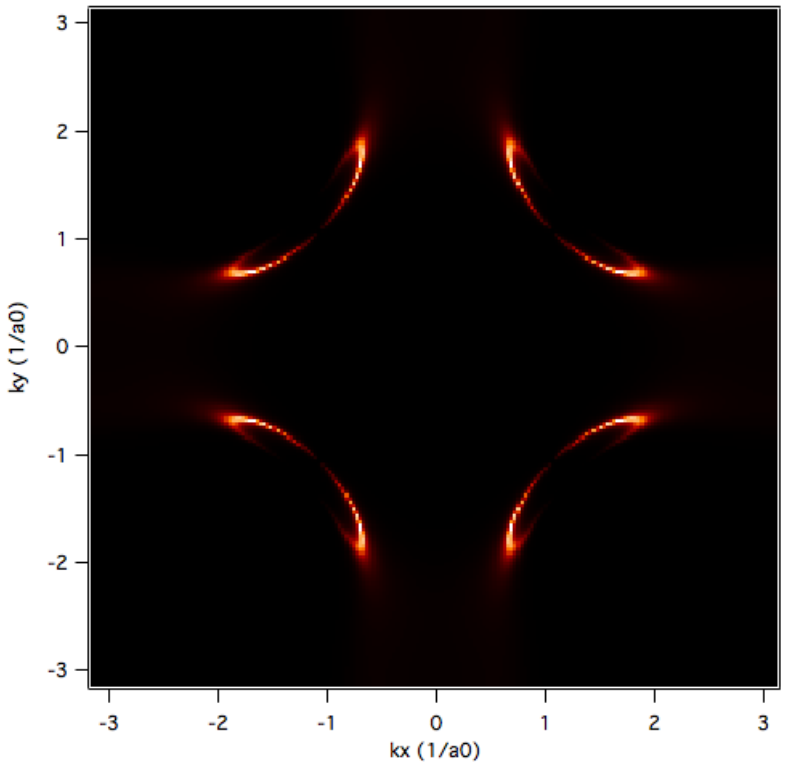

FIGURE 4.2: The spectral function of Bi-2212 using the Nambu-Gorkov formalism. This is a cut at $\omega = -12$ meV and at $T = 70K$ in the Fermi liquid phenomenology. The back bending and coherence factors are included in the formalism.

definition of Z where

$$Z = 1 - \frac{\Sigma' + i\Sigma''}{\omega}, \tag{4.3}$$

we have the renormalization factor for the five cuts in the Brillouin zone which is then interpolated. The renormalization factor is added into the Green's function to correct for the pairing of electrons and normalize the gap. Now that we have the full self energy, $\Sigma = \Sigma' + i\Sigma''$, we can include the self energy and the renormalization factor in the spectral function and autocorrelate.

4.2 Autocorrelation of the Spectral Function

An autocorrelation is a correlation of a function with itself, which is essentially looking at the similarities of the function as it is rolled over itself. For the spectral funciton, Eq. 2.9, this need to be done in three dimensions. An autocorrelation in general is,

$$C(t) = \int_{-\infty}^{\infty} \overline{E}(\tau)E(t+\tau)d\tau, \tag{4.4}$$

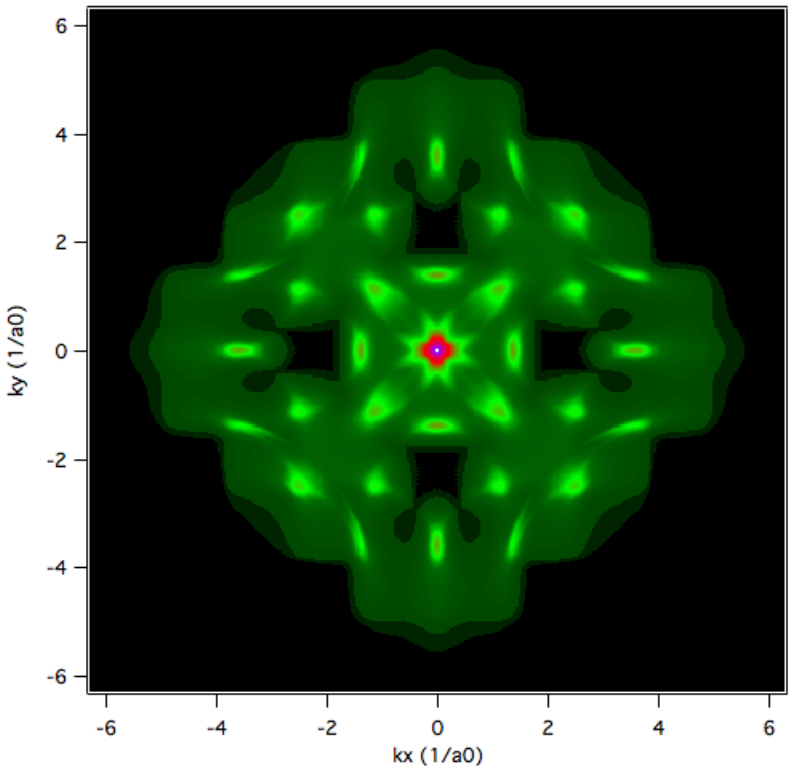

FIGURE 4.3: Here is an aurocorrelation of the band structure of Bi-2212 below the fermi surface, at $\omega = -12$ meV. The Fermi liquid phenomenology is used here with T=70 K. The peaks are directly related to the magnitudes and directions of the QPI vectors.

where $\overline{E}$ is the complex conjugate of some function. Unfortunately, an autocorrelation can take a very long time to compute. The brute force method of calculating is of order n^2 and with the data of approx. 200x200x250 we can see that this is not practical. Thankfully, there is a simplification to the autocorrelation, the Wiener-Khinchin theorem.

The Wiener-Khinchin theorem changes the autocorrelation from an integral to a multiplication of the Fourier transform of the spectral function. This simplification gives,

$$C(t) = \mathscr{F}^{-1}|\mathscr{F}(A(\mathbf{k},\omega)|^2), \tag{4.5}$$

where $\mathscr{F}$ is the Fourier transform of the function and $\mathscr{F}^{-1}$ is the inverse Fourier transform of the function [15]. This form of autocorrelation has a computation time of $n\log(n)$ which is a significant decrease in computation time from the brute force method.

The autocorrelation gives us a way of visualizing the QPI vectors in the Brillouin zone from the octet model. It is effectively a plot of $\mathbf{q}$-space where $\mathbf{q} = \mathbf{k}_f - \mathbf{k}_i$ In fig. 4.3, the peaks have 8-fold symmetry and the negative values are due to the electron being able to scatter both directions from the points of highest density of states. The labeling

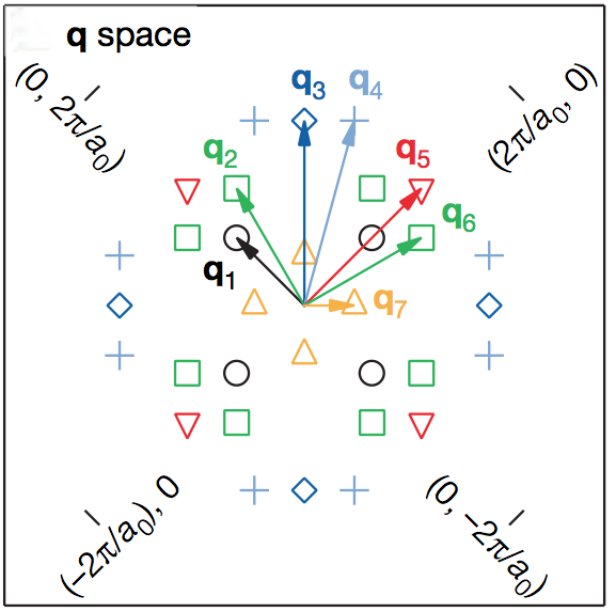

FIGURE 4.4: The q-space of Bi-2212 with all of the q-vectors depicted. This is rotated by 45 degrees from fig. 4.3 which is a product of STM groups having different conventions from ARPES groups [11].

of the q-vectors is done in fig. 4.4. The autocorrelation gives a simple way to track the changes of the **q**-vectors as a function of energy and temperature. Now we want to see how the magnitudes of the vectors change with respect to energy. From fig. 4.4, we can note that the $\mathbf{q}_3$ and $\mathbf{q}_7$ will always be on the 45 degree line while $\mathbf{q}_1$ and $\mathbf{q}_5$ will always be on the k_x axis.

4.2.1 Methods of Analysis

The DOS of states is calculated for each doping of PESE. This is done by counting all of the occupied states at each energy. The mapping of the magnitudes of the **q**-vectors can be done by taking a profile of the autocorrelation on the k_x axis and at a 45 degree angle to the k_x axis. Then, using the multi-peak fitting function in Igor, we can track the positions of the $\mathbf{q}_1, \mathbf{q}_3, \mathbf{q}_5$, and $\mathbf{q}_7$ vectors as a function of energy. We are looking to see if the relative properties of this simulation are consistent with the experimental STM data. Once we have done this, we can try to reconstruct the Fermi surface of Bi-2212.

Koshaka *et al* [11] gives the relations of the **q**-vectors to coordinates in the Brillouin zone, see Eq. 3.4. The symmetry of Bi-2212 allows us to use any two of the seven **q**-vectors to recreate the Fermi surface. Since it is only necessary to track two **q**-vectors because of the symmetry, the reconstruction of the positions are done two ways, using $\mathbf{q}_1, \mathbf{q}_5$ and $\mathbf{q}_3, \mathbf{q}_7$. This can then be compared to experimental data to check for consistency.

As the movement of QPI is tracked, the energy at which the profiles of the autocorrelation are collected. This allows for a recreation of the gap as a function of θ_k which is compared to the input gap,

$$\Delta(\theta_k) = \frac{\Delta_0}{2} \cos(\theta_k), \tag{4.6}$$

where Δ_0 is the maximum gap and θ_k is the angle measured from the corner of the Brillouin zone to the Fermi arcs where 0 degrees is defined as the node. This analysis is done for three doping simulations of PESE.

Chapter 5

Analysis

The analysis of simulations for Bi-2212 using the PESE phenomenology are discussed and physical explanations are determined. Three cases for doping in Bi-2212 are considered, under-doped at $\delta = 0.11$, optimal doping at $\delta = 0.16$, and over-doped at $\delta = 0.21$ are considered. All data is simulated with a temperature of 4 K to match the temperature of experimental STM data [8].

5.1 Self Energy

The PESE self energy has been calculated for $\alpha = \frac{1}{2}$ for an optimally doped sample. Since α is a linear fit, we can find values for different dopings of Bi-2212. For the simulation of the under-doped and over-doped PESE α is 0.479 and 0.568 respectively. Then, using these values for alpha, we can acquire the self energy at the five locations in k-space and interpolate (see fig. 5.1). These self energies are then put into the Green's function and autocorrelated. Using the techniques developed in Chapter 4, we can calculate the DOS, track the positions of the **q**-vectors, plot k_y vs. k_x, and analyze the output gap.

These cuts were provided by Haoxiang Li in simulation. It was also assumed that the constants associated with the self energy are constant as α is changed. This is a simplification and should be noted, since it is likely that the constants do change with changing α.

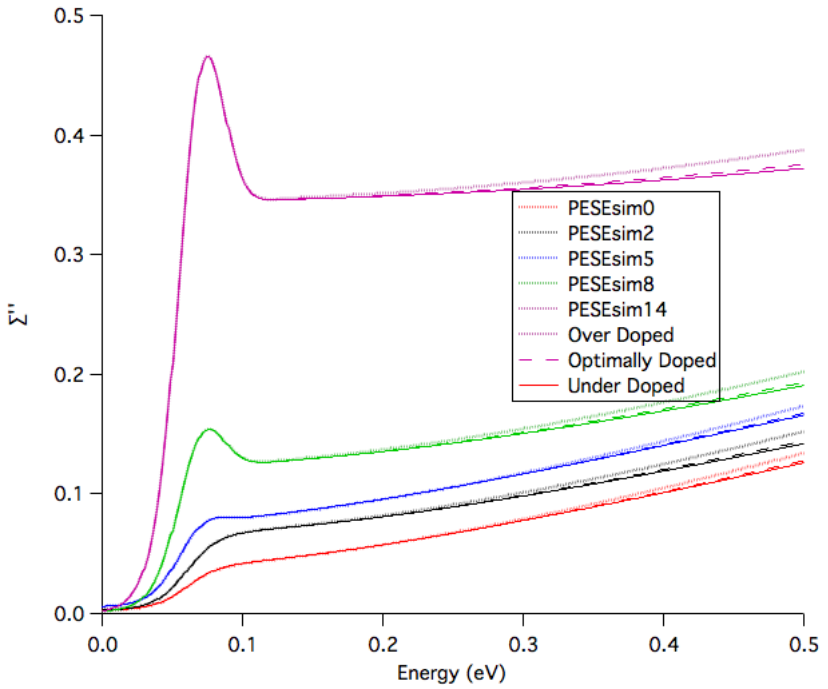

FIGURE 5.1: The cuts of the self energy for different spots in the Brillouin zone for the three doping simulations. The simulations are done at 5 points in the Brillouin zone. The node is defined as 0 degrees while the antinode is approx. 14 or 15 degrees. These cuts are interpolated and added to the greens function.

5.1.1 Calculated Density of States

The DOS is a good way to measure the gap value and make sure the renormalization factor is working. Since the doping of each simulation is different, we have to adjust the gap accordingly. The gap values are 20 meV, 25 meV, and 33 meV for the over-doped, optimally doped, and under-doped simulations respectively. These gap values are consistant with ARPES measurement for samples of these dopings (T. Reber *et al.* in review at PNAS). The gap values for the DOS of the under-doped sample show the gap is 30 meV and -30 meV for the positive and negative energy scale respectively. The renormalization factor is working correctly, since the DOS shows the same gap value as the input gap. Since the input gap is Eq. 2.7 the maximum will occur at the edge of the anti-ferromagnetic boundary. This will cause the magnitude of the gap at the anti-node to be a bit less than the input value. This effect is seen with measurement of the actual gap at the anti-node. The DOS also doesn't go to zero at the Fermi energy which is consistent with the self energy used because we have a constant broadening, Γ_0. There also appears to be other maximums (one on each side of the Fermi energy) (see Eq. 3.1). This feature is due to the physical change of the band due to the hump that is not accounted for in the Fermi liquid model (see fig. 5.2). There is a bump in the DOS at approximately -40 meV. This is caused by the kink in the self energy, but

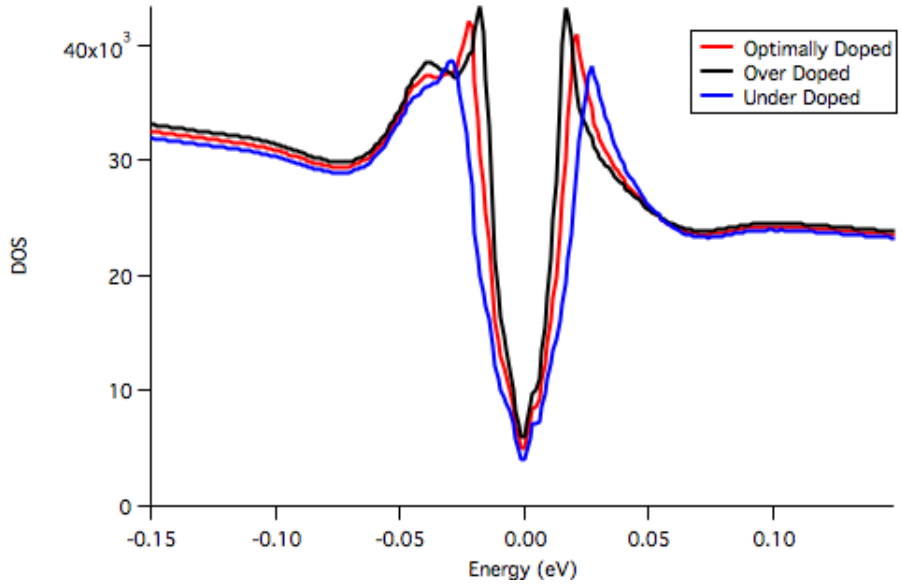

FIGURE 5.2: The density of states for Bi-2212 using the PESE self energy with a hump and a kink for the three doping simulations. This is calculated before the Oli Anderson matrix element is added to the spectral function, Eq. 2.10.

this effect is not symmetric because the bare band structure is not symmetric about the Fermi energy.

The optimally doped sample shows a gap value of 22 meV and -22 meV, which is consistent with its input gap. While the over-doped simulation gives the gap of approx. 17.5 meV and -17.5 meV which is consistent with its input gap. The two small bumps on each side of the Fermi energy are most likely due to the hump in the band structure. There is a bump due to the kink in the PESE, which is explained for the under-doped simulation and applies to the other simulations.

5.1.2 Tracking QPI Vectors

Tracking of the **q**-vectors has been done using the Fermi Liquid model and the PESE phenomenology. This is then compared to STM data. The Fermi liquid self energy gives similar slopes for the linear fits of the data (see fig. 5.3). An issue is the crossing points for the magnitudes of $\mathbf{q}_1, \mathbf{q}_7$ and $\mathbf{q}_3, \mathbf{q}_5$. The Fermi liquid simulation shows a crossing of approx. 21 meV and 23 meV for $\mathbf{q}_1, \mathbf{q}_7$ and $\mathbf{q}_3, \mathbf{q}_5$ respectively, while STM data shows a crossing of approx. 10 meV and less than 7 meV for $\mathbf{q}_1, \mathbf{q}_7$ and $\mathbf{q}_3, \mathbf{q}_5$ respectively. This difference is resolved with the new self energy.

The magnitudes of the **q**-vectors are tracked using the PESE model and are compared to the STM data. First, looking at the under-doped sample, we can see that the slopes are roughly a factor of two above the slopes shown in the STM data. The main difference

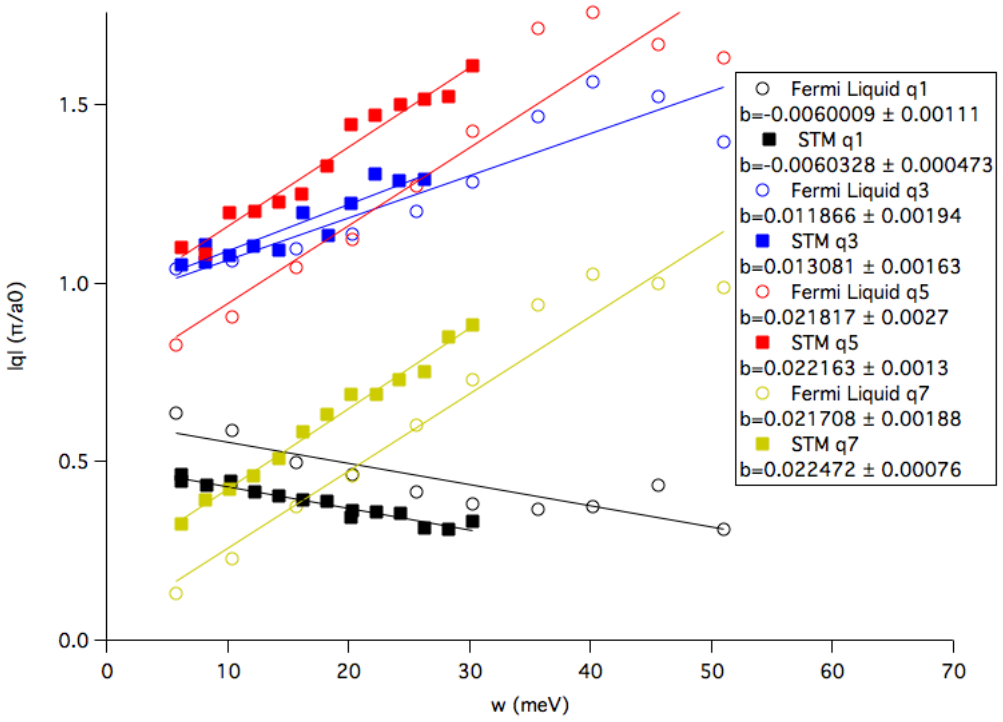

FIGURE 5.3: The magnitudes of the **q**-vectors tracked with increasing energy for the STM data in [8] and Fermi liquid self energy using the tight binding band structure. The slopes are similar, but the crossing of each pair of **q**-vectors is greater than the STM data.

is the intersections of the fitted data are closer to the STM data. The intersections are approx. 10 meV and 10 meV for $\mathbf{q}_1, \mathbf{q}_7$ and $\mathbf{q}_3, \mathbf{q}_5$ respectively.

The optimally doped sample has fitted slopes that are still a factor of 3 greater than the STM data. The intersections are at approx. 7 meV and 8 meV for $\mathbf{q}_1, \mathbf{q}_7$ and $\mathbf{q}_3, \mathbf{q}_5$ respectively. The intersections of the over-doped sample $\mathbf{q}_1, \mathbf{q}_7$ and $\mathbf{q}_3, \mathbf{q}_5$ fitted data are approx. 6 meV and 7 meV respectively. While the slopes are still factors of roughly 2 or 3 greater than the STM data. A possible explaination could be the real part of the self energy. When this is included in the spectral function physically changes the shape of the band and shifts the spectral weight. This will in turn cause a shift in the peaks of the **q**-vectors. This effect didn't happen for the Fermi Liquid slopes (see fig. 5.3) because the tight binding band structure was used and this is already fitted to include the real part of the self energy [16].

5.1.3 Reconstructing the Band Structure from QPI

Using the methods described in Chapter 4 the positions of the **q**-vectors can be plotted in **k**-space. In fig. 5.8, the k_x and k_y momentums for the two different methods are plotted for an under-doped sample. The Fermi surface is included to show the path

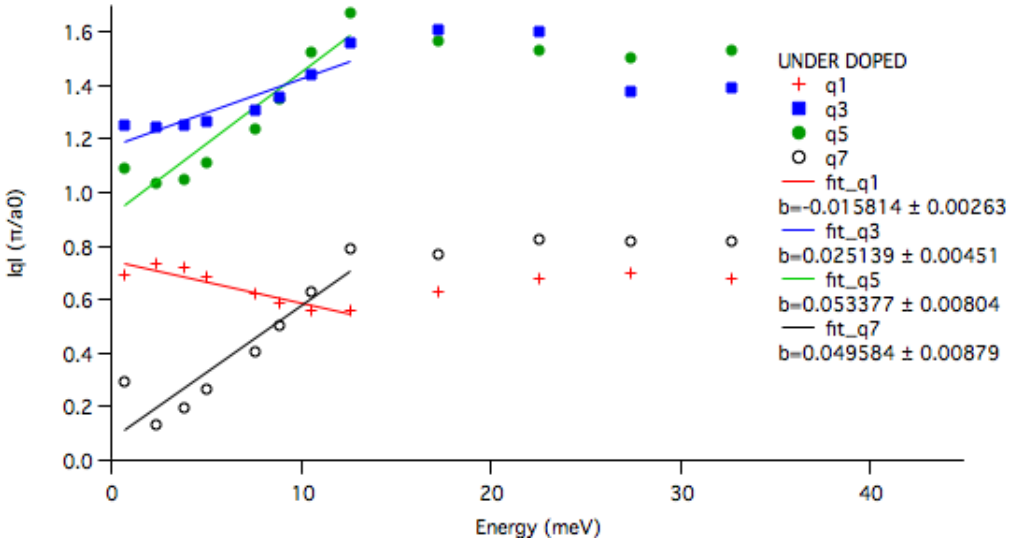

FIGURE 5.4: The magnitudes of the **q**-vectors tracked for the under-doped simulation using PESE. The intersection of the pairs of **q**-vectors match the STM data well, but the slopes are a factor of 2 greater.

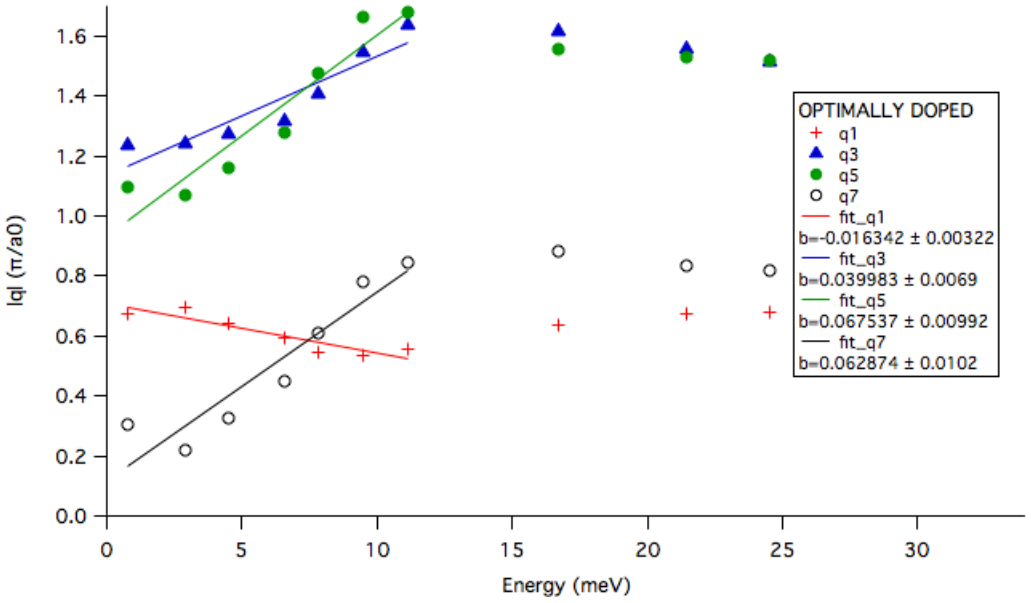

FIGURE 5.5: The magnitudes of the **q**-vectors tracked for the optimally doped simulation with PESE. Like the under-doped simulations the intersections of the **q**-vectors are similar to the STM data.

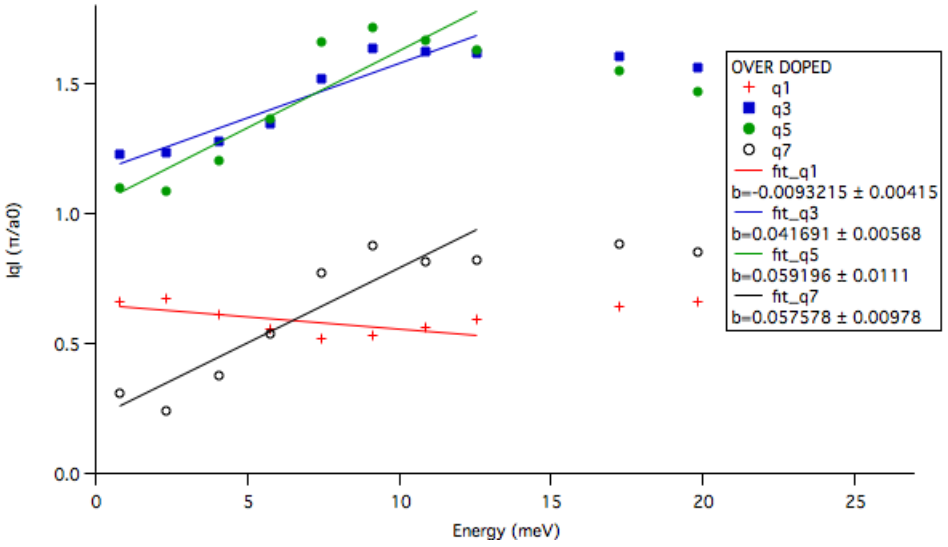

FIGURE 5.6: The magnitudes of the **q**-vectors are tracked for the over-doped simulation with PESE. The interestions of the **q**-vectors is close to the STM data.

that the positions should follow. The positions are expected to be on the inside of each quarter circle since the measurements were taken above the Fermi energy. The positions stop after the anti-ferromagnetic zone boundary, which is mentioned in Chapter 3. This effect is seen in this self energy phenomenology and in a reconstruction using a Fermi liquid self energy. This effect is most likely caused by the real part of the self energy. The real Σ' changes the spectral weight of the band structure in the opposite way that the superconducting gap does. This will cause the autocorrelations to track the peaks of the new shifted spectral weight.

The positions of the k_x and k_y momentum for the optimally doped case can be seen in fig. 5.9. The positions of the momentums also stop after the anti-ferromagnetic zone boundary. In fig. 5.10, we see that the positions of the momentums stop after the anti-ferromagnetic zone boundary for the over-doped sample. The **q** cannot be tracked any further because there is too much broadening for the self energy. The stationary effect of the positions of the **q**-vectors should be seen when at the gap and above, but this effect is seen starting at about 15 meV for each doping. The Fermi liquid reconstruction is shown in fig. 5.7 where there is also a bunching of positions at the gap value and above since for this data the tight binding model was used and the real part of the self energy was not needed.

5.1.4 Output gap

The positions of the momentums can be altered into an angle with the origin being one of the corners of the Brillouin zone. This is then compared to the input superconducting

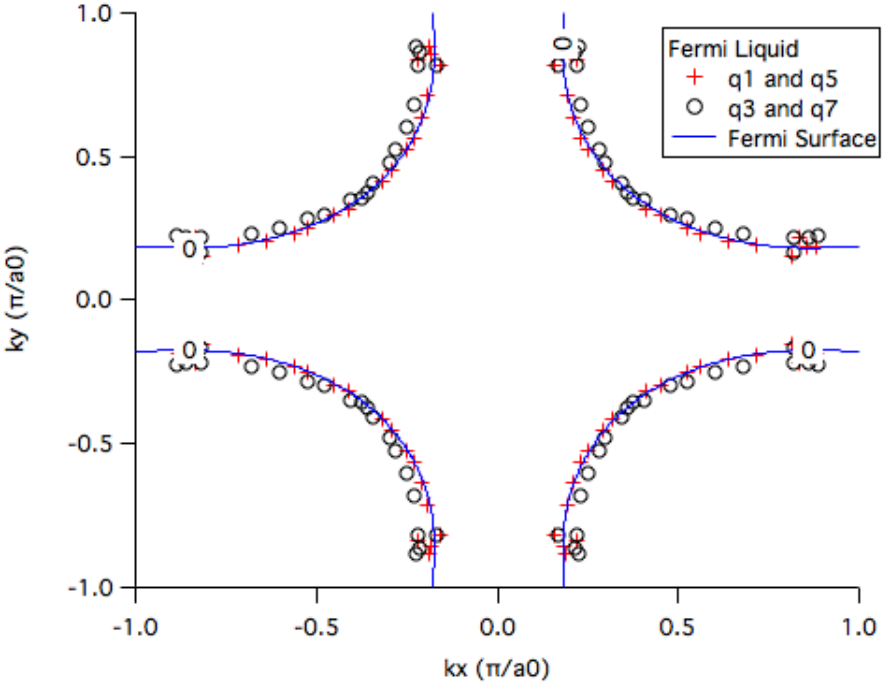

FIGURE 5.7: The Fermi liquid self energy is used along with the tight binding band structure to track the QPI in the superconducting gap. This is done using two different pairs of **q**-vectors.

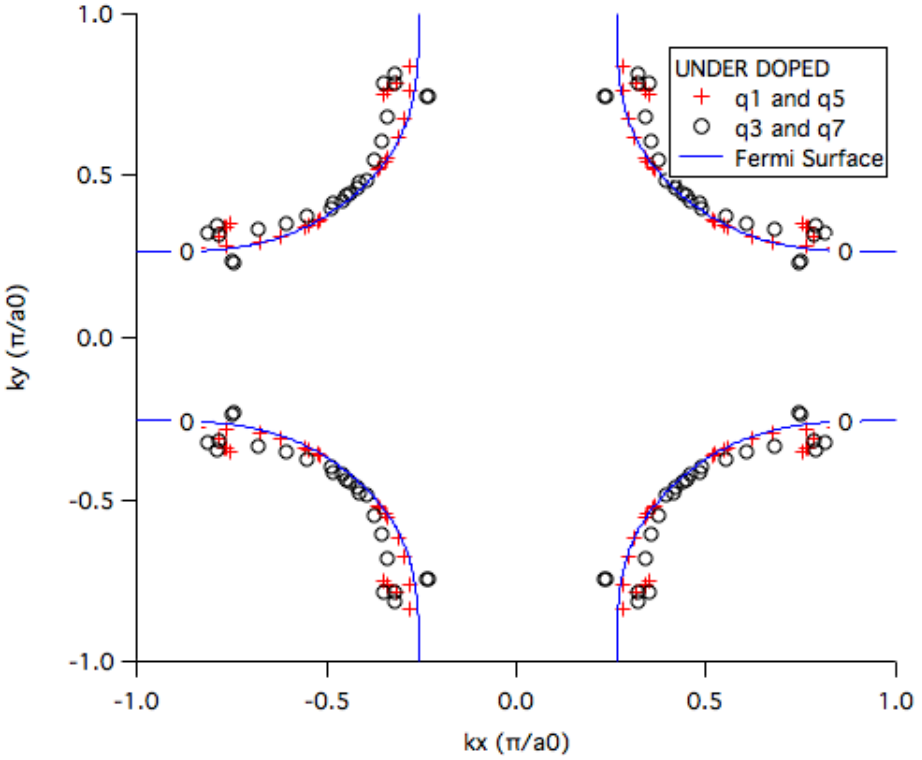

FIGURE 5.8: This is the recreation of the band structure for an under-doped sample. The locations of the points were found using two different pairs of **q**-vectors. Added is a contour of the bare band structure at the Fermi energy.

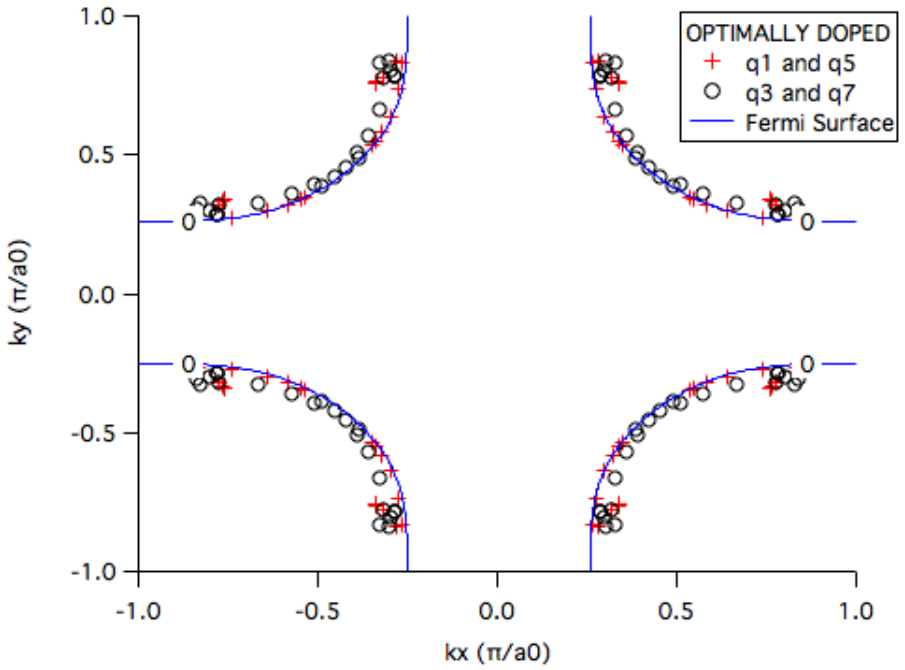

FIGURE 5.9: This is the recreation of the band structure for an optimally doped sample. The locations of the points were found using two different pairs of **q**-vectors. Added is a contour of the bare band structure at the Fermi energy.

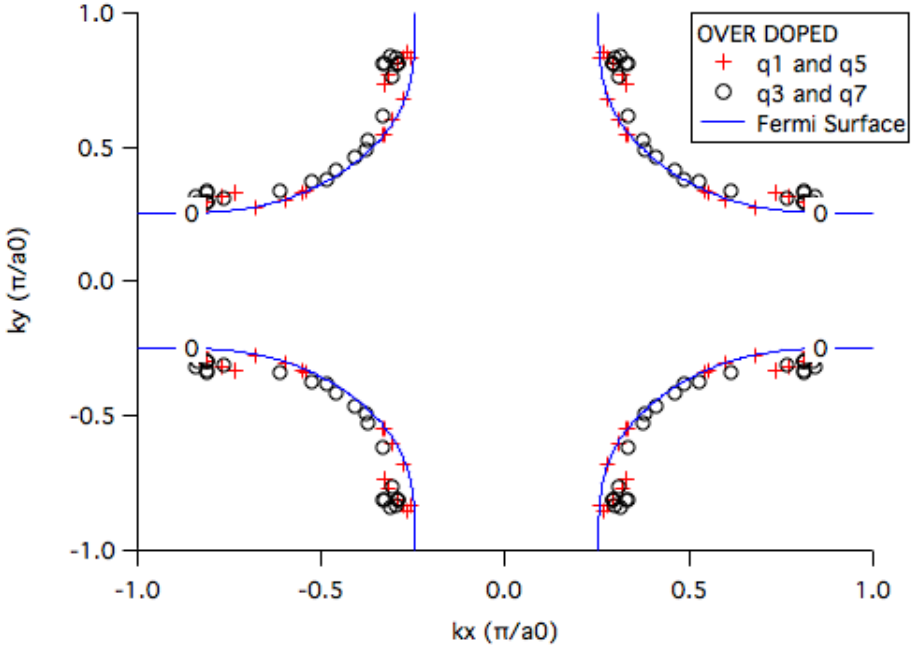

FIGURE 5.10: This is the recreation of the band structure for an over-doped sample. The locations of the points were found using two different pairs of **q**-vectors. Added is a contour of the bare band structure at the Fermi energy.

gap. If we compare fig. 5.12, 5.13, and 5.14 we can see the **q**-vectors do not accurately recreate the superconducting gap. The reconstruction was done using two methods, $\mathbf{q}_1, \mathbf{q}_5$ and $\mathbf{q}_3, \mathbf{q}_7$. These are then compared to the reconstruction of the gap using a constant broadening of 3 meV (see fig. 5.11).

The $\mathbf{q}_1, \mathbf{q}_5$ construction appears to be going to the node at the Fermi energy, but collapsed at the node. The $\mathbf{q}_3, \mathbf{q}_7$ construction appears to collapse before the node. In Chapter 3, it was stated that the the temperature dependence of QPI shows the superconducting gap closes near the node. Here, we are only looking at one temperature, 4 K. Although, the $\mathbf{q}_3, \mathbf{q}_7$ construction of the gap closes near the node it is necessary to acquire more data to show conclusive evidence of the gap collapsing at the node. There is a fundamental difference in the reconstruction techniques used in this analysis. The data using the $\mathbf{q}_1, \mathbf{q}_5$ is fundamentally different than the $\mathbf{q}_3, \mathbf{q}_7$ data. The symmetry of the band structure indicates that this should not be the case; it may be possible to see this effect again by using different combinations of the four **q**-vectors. In all of the doping simulations, the QPI reconstructions seem to be approaching a value of the gap that is roughly half of the input gap. Since the constant broadening is able to accurately recreate the gap, this implies that the strength of the real part of the gap is causing the disagreement. As previously mentioned the real part of Σ changes the spectral weight of the band structure and this will cause the positions of the **q**-vectors to be skewed. Further analysis is needed to see if this is indeed true. Another solution to the discrepancies seen between the DOS and the recreation of the gap using QPI could be fixed by fitting the tight binding band structure that Haoxiang Li is using with the real part of the self energy that we are using. This would allow for a simpler spectral function since we would only need to include the imaginary part of the self energy, Σ'' and we could neglect the renormalization, Z. The only problem with this method is that the fitting is for individual dopings of Bi-2212. This would mean we need three different fitted tight binding band structures.

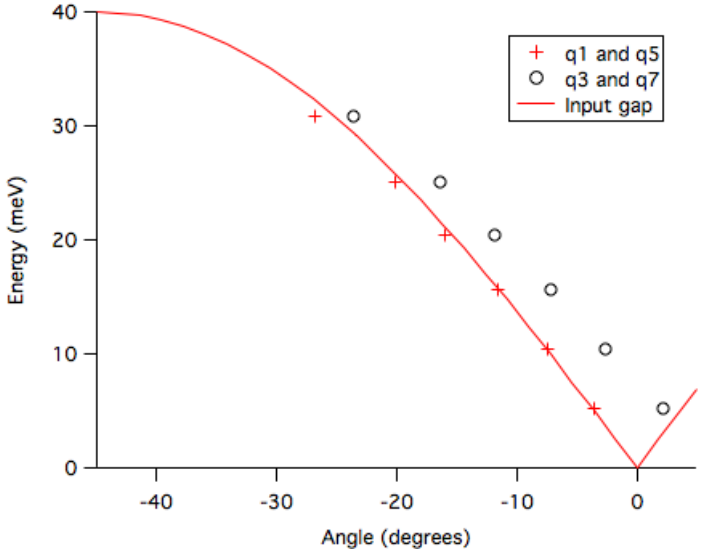

FIGURE 5.11: The recreation of the superconducting gap using a constant self energy of 3 meV. The tight binding band structure was used in this simulation. The recreation was again done using two methods, $\mathbf{q}_1, \mathbf{q}_5$ and $\mathbf{q}_3, \mathbf{q}_7$. The node is defined as 0 degrees and the anti-node is 45 degrees.

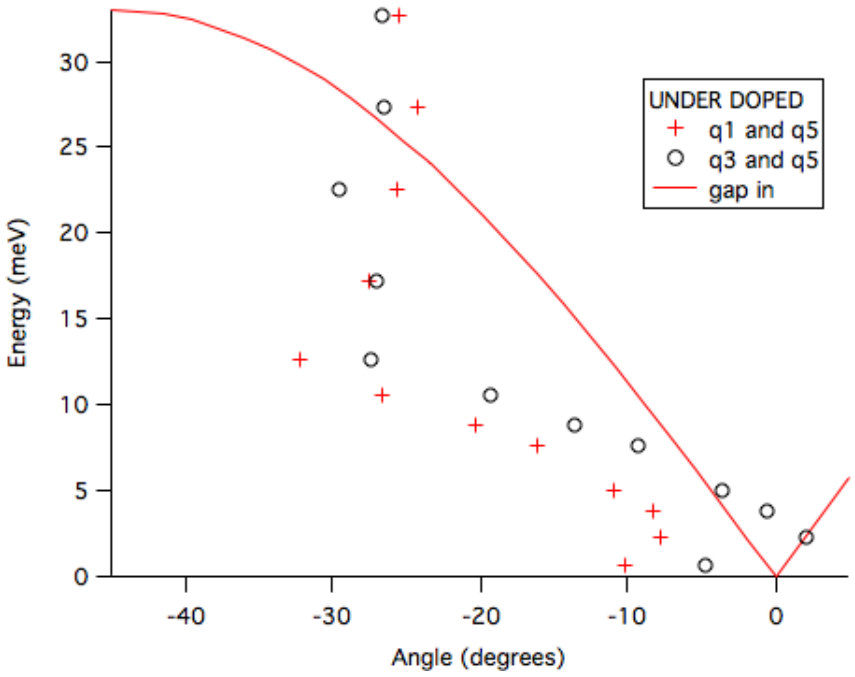

FIGURE 5.12: The **q**-vectors are used to recreate the superconducting gap. This was done two separate ways with two different pairs of **q**-vectors. The angle is defined such that 0 degrees is the node and 45 degrees is the anti-node. Since the gap is symmetric about the node it is only necessary to show half of it. The input gap is also shown as a comparison.

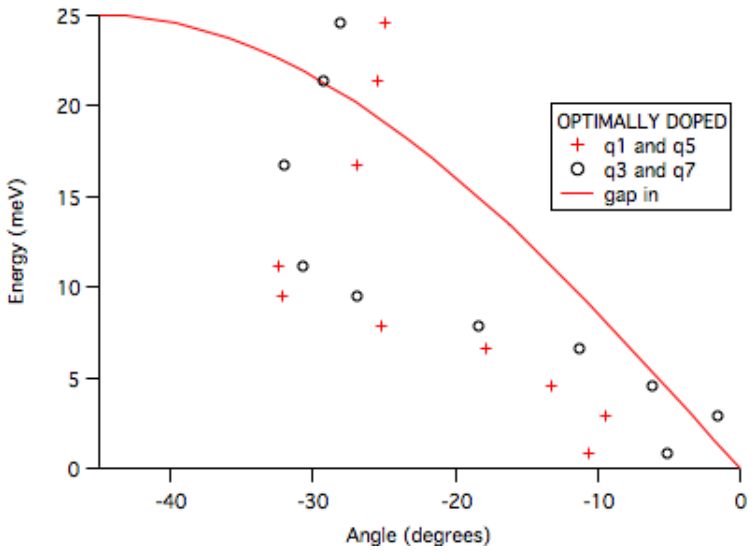

FIGURE 5.13: The **q**-vectors are used to recreate the superconducting gap. This was done two separate ways with two different pairs of **q**-vectors. The angle is defined such that 0 degrees is the node and 45 degrees is the anti-node. Since the gap is symmetric about the node it is only necessary to show half of it. The input gap is also shown as a comparison.

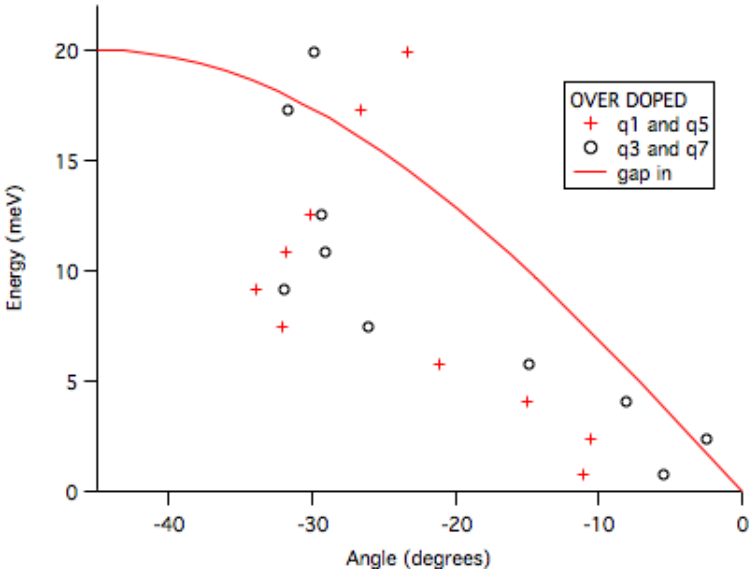

FIGURE 5.14: The **q**-vectors are used to recreate the superconducting gap. This was done two separate ways with two different pairs of **q**-vectors. The angle is defined such that 0 degrees is the node and 45 degrees is the anti-node. Since the gap is symmetric about the node it is only necessary to show half of it. The input gap is also shown as a comparison.

Chapter 6

Conclusion

The PESE phenomenology looks promising as a self energy to describe Bi-2212 and possible other cuprate superconductors. The slopes of the **q**-vectors are a factor of about 2 to 3 greater than the STM data. The crossing points between the pairs of vectors, $\mathbf{q}_1, \mathbf{q}_7$ and $\mathbf{q}_3, \mathbf{q}_5$ match the experimental data well, much better than the Fermi liquid model of the self energy. The recreations of the positions of the **q**-vectors match the Fermi surface for each doping. There is a bunching of states after the anti-ferromagnetic zone boundary. This is also seen in the Fermi liquid reconstruction. The Fermi liquid bunching occurs at energies above the gap, and the bunching for the PESE model occurs at energies of approx. 15 meV depending on the doping which is inside the gap. It was mentioned earlier in Chapter 5 that this effect could be due to the real self energy adding spectral weight to the band structure. This needs to be explored further before more analysis.

The DOS of each doping shows the correct gap which indicates that the set up of each simulation was done correctly. It is also possible to see the effects of the kink and the hump in the PESE phenomenology that is used. The asymmetry is explained by the asymmetry in the bare band structure of Bi-2212. The gap is then reconstructed using the two methods explained in Chapter 4. Near the Fermi energy, both recreations seem to collapse near the node at an angle of approx. 10 degrees and 5 degrees for the $\mathbf{q}_1, \mathbf{q}_5$ and $\mathbf{q}_3, \mathbf{q}_7$ recreations respectively. This cannot be confirmed to be an artifact of PESE, since the simulations were only done at one temperature, 4 K. The positions of the **q**-vectors is relatively constant above approx. 15 meV for each doping. This effect causes the bunching of positions seen in fig. 5.8, 5.9, 5.10.

The PESE phenomenology needs to have a couple problems checked to see if this data is an artifact of the self energy or the band structure. Future work is needed to provide a more complete analysis of PESE.

6.1 Future Work

The real part of the self energy could be fitted to the tight binding band structure for Bi-2212. This could possible solve the problem of the DOS and QPI reconstruction of the gap disagreeing. If this does not then solve the problem we could look for the contribution from the real self energy. The autocorrelation of the spectral function should be done algebraically to see where the real self energy contributes. The skewing of the real part of the PESE may then be accounted for and adjusted to see if this will correct the fact that the QPI and DOS calculations of the gap are different. Finding the real contribution of the self energy is something that no one appears to have done before and would possibly be noteworthy physics. Once we might have a correction for the self energy, there are many more variables to test.

These simulations could be done for other doping values to check for consistencies in the slopes and crossing points of the $\mathbf{q}$-vectors. Then, each doping simulations can be done at multiple temperatures in an attempt to show the collapsing gap at the node that is consistent with experiment [11]. A look into the fundamental difference in the appearance of the $\mathbf{q}_1, \mathbf{q}_5$ and $\mathbf{q}_3, \mathbf{q}_7$ recreations. The difference can be seen in the positions of the $\mathbf{q}$-vectors and the recreation of the gap. These effects could possibly be explained with PESE, but more analysis is needed.

Bibliography

[1] T. Senthil, Physical Review B **78** (2008), 10.1103/PhysRevB.78.035103, arXiv:0803.4009 [cond-mat].

[2] I. M. Vishik, E. A. Nowadnick, W. S. Lee, Z. X. Shen, B. Moritz, T. P. Devereaux, K. Tanaka, T. Sasagawa, and T. Fujii, Nature Physics **5**, 718 (2009), WOS:000271185400010.

[3] D. L. Maslov, arXiv:cond-mat/0506035 (2005).

[4] P. B. Littlewood and C. M. Varma, Journal of Applied Physics **69**, 4979 (1991).

[5] G. D. Mahan, *Many-Particle Physics* (Springer, 2000).

[6] R. S. Markiewicz, S. Sahrakorpi, M. Lindroos, H. Lin, and A. Bansil, Physical Review B **72**, 054519 (2005).

[7] J. R. Schrieffer, *Theory of Superconductivity* (Westview Press, 1999).

[8] K. McElroy, R. W. Simmonds, J. E. Hoffman, D.-H. Lee, J. Orenstein, H. Eisaki, S. Uchida, and J. C. Davis, Nature **422**, 592 (2003).

[9] J. E. Hoffman, Reports on Progress in Physics **74** (2011), 10.1088/0034-4885/74/12/124513, WOS:000298079500014.

[10] J. E. Hoffman, K. McElroy, D.-H. Lee, K. M. Lang, H. Eisaki, S. Uchida, and J. C. Davis, Science **297**, 1148 (2002), PMID: 12142440.

[11] Y. Kohsaka, C. Taylor, P. Wahl, A. Schmidt, J. Lee, K. Fujita, J. W. Alldredge, K. McElroy, J. Lee, H. Eisaki, S. Uchida, D.-H. Lee, and J. C. Davis, Nature **454**, 1072 (2008).

[12] J. Lee, K. Fujita, A. R. Schmidt, C. K. Kim, H. Eisaki, S. Uchida, and J. C. Davis, Science **325**, 1099 (2009), PMID: 19713522.

[13] C. V. Parker, P. Aynajian, E. H. da Silva Neto, A. Pushp, S. Ono, J. Wen, Z. Xu, G. Gu, and A. Yazdani, Nature **468**, 677 (2010).

[14] S. H. Hall and H. L. Heck, *Advanced Signal Integrity for High-Speed Digital Designs* (John Wiley & Sons, 2011).

[15] C. Chatfield, *The Analysis of Time Series: An Introduction, Sixth Edition* (CRC Press, 2013).

[16] M. R. Norman, Physical Review B **61**, 14751 (2000).